



# Martensitic Transformation in Stainless Steels

Ye Tian

Doctoral Thesis

Department of Materials Science and Engineering  
School of Industrial Engineering and Management  
KTH Royal Institute of Technology  
SE-100 44 Stockholm  
Sweden

---

Akademisk avhandling som med tillstånd av Kungliga Tekniska Högskolan i Stockholm, framlägges för offentlig granskning för avläggande av Teknologie Doktorsexamen, torsdagen den 14 juni 2018, kl. 10:00 i Kollegiesalen, Brinellvägen 8, Kungliga Tekniska Högskolan, Stockholm.

---

ISBN 978-91-7729-786-4

Ye Tian

Martensitic Transformation  
in Stainless Steels

Department of Materials Science and Engineering

School of Industrial Engineering and Management

KTH Royal Institute of Technology

SE-100 44 Stockholm

Sweden

ISBN: 978-91-7729-786-4

© Ye Tian (田野)

This thesis is available in electronic version at [kth.diva-portal.org](http://kth.diva-portal.org)

Printed by Universitetservice US-AB, Stockholm, Sweden

## ABSTRACT

Metastable austenite ( $\gamma$ ) can be transformed to the thermodynamically more stable  $\alpha'$ -martensite ( $\alpha'$ ) during deformation. This is usually termed deformation-induced martensitic transformation (DIMIT). DIMIT is considered to be responsible for the substantial ductility enhancement in the transformation-induced plasticity (TRIP) related steels. Therefore, this work aims to investigate DIMIT in metastable austenitic stainless steels, which are good model materials without the interference of other phases. The follow-up work extends the investigation to multiphase steels, *i.e.* TRIP-assisted duplex stainless steels (TDSS). The main focuses are the deformation mechanisms and related crystallography of both stainless steels.

In austenitic Fe-Cr-Ni model alloys, the transformation sequence from  $\gamma$  to  $\alpha'$  was visualized during *in situ* incremental cooling using grain-averaged and single-grain analysis based on high-energy X-ray diffraction (HEXRD). The results indicate that the transient phase is  $\epsilon$ -martensite ( $\epsilon$ ) with stacking faults as precursors. In the deformation case, the deformation microstructure and deformation-induced  $\alpha'$  were observed and correlated with stacking fault energy (SFE). The results include that the role of  $\epsilon$  in the formation of  $\alpha'$  is similar to that in cooling experiment.  $\alpha'$  units nucleate adjacent to  $\epsilon$  within individual shear bands and their intersections in low SFE alloys. The small  $\alpha'$  variants observed within individual shear bands are mainly twin-related due to an autocatalytic behavior that minimize the transformation strain energy. In alloys with higher SFEs, the variant selection behaviour is seen due to the favorable stress/strain field. The Schmid's law and Bogers-Burgers double shear mechanism can be used to estimate this selective manner. The formation of  $\epsilon$  is further restricted in alloys with much higher SFEs. In this case, the individual shear bands consisting of mainly mechanical twins are not potential sites for  $\alpha'$  formation and thus require intersecting shear bands.

In TDSS, samples with three different stabilities of the  $\gamma$  phase, were investigated by HEXRD during *in situ* uniaxial tensile loading. A deformation microstructure dependence on SFE is found, which is similar to what we observed in Fe-Cr-Ni model alloys. The micromechanics, however, is much more complicated due to the influence of the continuous formation

of  $\alpha'$  and related interactions with other constituent phase during deformation. The initial load partitioning is associated with the yield strengths of individual phases. A major load transfer occurs at the point where maximum  $\alpha'$  transformation takes place, and a work hardening is clearly seen in alloys with the most unstable  $\gamma$  due to the pronounced TRIP effect. One grade was selected for studying the orientation dependency of the mechanical stability of  $\gamma$ . This analysis was based on texture and individual grain analysis using electron backscatter diffraction. The Schmid's law and double shear mechanism are shown to be applicable to explain the mechanical stability of  $\gamma$  in terms of the orientation difference in TDSS. It is found that the activation of multiple slip planes is important for the formation of  $\alpha'$  at a certain applied stress.

## **KEYWORDS**

Metastable austenitic stainless steels; TRIP-assisted duplex stainless steels; Martensitic transformation; Deformation mechanism; Stacking fault energy; *In situ* investigation.

## Sammanfattning

Deformationsinducerad martensitisk fasomvandling (DIM) anses vara ansvarig för förbättringen av duktiliteten i s.k. TRIP stål. I den här avhandlingen undersöks metastabila austenitiska rostfria stål som är bra modellmaterial för att studera DIM utan influens från andra faser. Vidare undersöks även mer komplexa rostfria stål med två ingående faser, austenit och ferrit, där austeniten är metastabil och ger en TRIP effekt, dessa stål kallas duplexa TRIP stål. I austenitiska Fe-Cr-Ni-modelllegeringar studerades omvandlingen från austenit ( $\gamma$ ) till  $\alpha'$ -martensit ( $\alpha'$ ) in situ under kylning m.h.a. högenergiröntgendiffraktion. Omvandlingen från  $\gamma$  till  $\alpha'$  sker via staplingsfel och  $\epsilon$ -martensit ( $\epsilon$ ). Detta indikerar att genereringen av potenta kärnbildningsställen kan stimulera DIM. Bildandet av DIM studerades också efter deformation och korrelerades med staplingsfelsenergin (SFE) hos austeniten.  $\alpha'$  bildas inom skjuvband samt vid skärningpunkter mellan skjuvband i legeringar med låg SFE. Enheterna av  $\alpha'$  som bildas är tvillingorienterade till varandra för att minimera töjningsenergin. Schmid's lag och Bogers-Burgers dubbla skjuvmekanism kan användas för att förutsäga de kristallografiska varianterna som bildas. Omvandlingen till  $\epsilon$  är begränsad vid hög SFE och då består skjuvbanden i huvudsak av deformationstvillingar. I det fallet så är det svårare att bilda  $\alpha'$  och skärningpunkter mellan skjuvband är därför nödvändiga för att bilda  $\alpha'$ . Två duplexa TRIP legeringar undersöktes under in situ enaxlig dragprovning och deformationsstrukturen hos austeniten liknar den hos austenitiska modellegeringar. Mikromekanismen hos dessa stål är dock mycket mer komplicerad än hos de enfasiga modellegeringarna. Den initiala lastfördelningen mellan austeniten och ferriten förändras dramatiskt när  $\alpha'$  bildas, framförallt när bildandet är som störst. En tydlig TRIP effekt kunde observeras i de duplexa TRIP stålen. Strukturen efter deformation analyserades sen vidare m.h.a. EBSD. Orienteringsberoendet på austenitens stabilitet studerades och kunde beskrivas m.h.a. Schmid's lag och Bogers-Burgers mekanism. Aktiveringen av flera glidsystem är viktig för bildandet av  $\alpha'$ .



## SUPPLEMENTS

The thesis is based on the following papers:

Paper I: “Martensite formation during incremental cooling of Fe-Cr-Ni alloys: An in-situ bulk X-ray study of the grain-averaged and single-grain behavior”

**Ye Tian**, Ulrich Lienert, Annika Borgenstam, Torben Fischer, and Peter Hedström

Scripta Materialia, 2017, vol. 136, pp. 124-127

Paper II: “Deformation microstructure and deformation-induced martensite in austenitic Fe-Cr-Ni alloys depending on stacking fault energy”

**Ye Tian**, Oleg I. Gorbatov, Annika Borgenstam, Andrei V. Ruban, and Peter Hedström

Metallurgical and Materials Transactions A, 2017, vol. 48, pp. 1-7.

Paper III: “Comparing the deformation-induced martensitic transformation with the athermal martensitic transformation in Fe-Cr-Ni alloys”

**Ye Tian**, Annika Borgenstam, Peter Hedström

Submitted manuscript.

Paper IV: “Micromechanics and microstructure evolution during *in situ* uniaxial tensile loading of TRIP-assisted duplex stainless steels”

**Ye Tian**, Sen Lin, Peter Ko, Ulrich Lienert, Annika Borgenstam, and Peter Hedström

Submitted manuscript.

Paper V: “Mechanical stability of austenite grains towards martensitic transformation in a TRIP-assisted duplex stainless steel”

**Ye Tian**, Yadunandan B. Das, Annika Borgenstam,  
Peter Hedström  
In manuscript.

**Other related papers not included in the thesis:**

1. “A microstructural investigation of athermal and deformation-induced martensite in Fe-Cr-Ni alloys”  
**Ye Tian**, Annika Borgenstam, and Peter Hedström  
Materials Today: Proceedings, 2015, vol. 2, pp. 687-690.

**The contributions by the author to the papers:**

- Paper I: Major parts of literature survey, experiments, data analysis and paper writing;
- Paper II: Major parts of literature survey, experiments, data analysis and paper writing; the first-principles calculations were done by the collaborators.
- Paper III: Major parts of literature survey, experiments, data analysis and paper writing;
- Paper IV: Major parts of literature survey, experiments, data analysis and paper writing;
- Paper V: Major parts of literature survey, experiments, data analysis and paper writing;

# CONTENTS

<b>1</b>	<b>INTRODUCTION.....</b>	<b>1</b>
1.1	SCOPE OF PRESENT WORK.....	2
<b>2</b>	<b>DEFORMATION BEHAVIOR OF TRIP-ASSISTED STAINLESS STEELS.....</b>	<b>5</b>
2.1	DEFORMATION IN AUSTENITIC STAINLESS STEELS .....	6
2.2	DEFORMATION IN MULTIPHASE STAINLESS STEELS.....	7
2.3	DEFORMATION-INDUCED MARTENSITIC TRANSFORMATION (DIMIT) .....	8
2.3.1	<i>Martensite formation and related crystallography</i> .....	8
2.3.2	<i>Thermodynamics and kinetics</i> .....	10
2.3.3	<i>Stacking fault energy</i> .....	12
2.3.4	<i>Factors affecting deformation-induced martensitic transformation</i> .....	13
<b>3</b>	<b>EXPERIMENTAL METHODS.....</b>	<b>15</b>
3.1	MATERIALS AND SAMPLE PREPARATIONS .....	15
3.2	MICROSTRUCTURAL CHARACTERIZATION .....	17
3.2.1	<i>Light optical microscopy (LOM)</i> .....	17
3.2.2	<i>Scanning electron microscopy (SEM)</i> .....	17
3.3	HIGH-ENERGY X-RAY DIFFRACTION (HEXRD).....	22
3.3.1	<i>Synchrotron radiation</i> .....	22
3.3.2	<i>In situ environment</i> .....	22
3.3.3	<i>Experimental setup</i> .....	23
3.3.4	<i>Data analysis</i> .....	24
3.3.5	<i>Three-dimensional X-ray diffraction (3DXRD)</i> .....	26
<b>4</b>	<b>SUMMARY OF APPENDED PAPERS .....</b>	<b>29</b>
4.1	FE-CR-NI MODEL ALLOYS .....	29
4.1.1	<i>Martensite formation during in situ cooling experiments (Paper I)</i> .....	29
4.1.2	<i>The deformation microstructure and deformation-induced martensite depending on SFE (Paper II)</i> .....	30
4.1.3	<i>Comparing the deformation-induced martensitic transformation with the athermal martensitic transformation in Fe-Cr-Ni alloys (Paper III)</i> .....	31
4.2	TRIP-ASSISTED DUPLEX STAINLESS STEELS.....	32
4.2.1	<i>Micromechanics and microstructure evolution during in situ uniaxial tensile loading of TRIP-assisted duplex stainless steels (Paper IV)</i> .....	32
4.2.2	<i>Mechanical stability of austenite grains towards martensitic transformation in a TRIP-assisted duplex stainless steel (Paper V)</i> .....	33
<b>5</b>	<b>CONCLUDING REMARKS AND FUTURE WORK .....</b>	<b>35</b>
5.1	CONCLUDING REMARKS .....	35
5.2	FUTURE WORK .....	36

<b>ACKNOWLEDGEMENTS.....</b>	<b>39</b>
<b>BIBLIOGRAPHY .....</b>	<b>41</b>

# LIST OF ABBREVIATIONS

$\alpha$	Ferrite
$\gamma$	Austenite
$\varepsilon$	$\varepsilon$ -martensite
$\alpha'$	$\alpha'$ -martensite
SFE	Stacking fault energy
DIMT	Deformation-induced martensitic transformation
TDSS	TRIP-assisted duplex stainless steels
ECCI	Electron channeling contrast imaging
EBSD	Electron backscatter diffraction
SEM	Scanning electron microscopy
HEXRD	High-energy X-ray diffraction
3DXRD	Three-dimensional X-ray diffraction
TRIP	Transformation-induced plasticity
<i>fcc</i>	Face-centered cubic
<i>hcp</i>	Hexagonal close-packed
OR	Orientation relationships
KS-OR	Kurdjumov-Sachs orientation relationship
NW-OR	Nishiyama-Wasserman orientation relationship
XRD	X-ray diffraction
LOM	Light optical microscopy
FE-SEM	Scanning electron microscopy with a field emission gun
EDS	Energy dispersive spectroscopy
TEM	Transmission electron microscopy
FIB	Focused ion beam



# 1 INTRODUCTION

Albert Einstein:

*“[I do not] carry such information in my mind since it is readily available in books. ...The value of a college education is not the learning of many facts but the training of the mind to think.”*

Stainless steels are of great importance due to their extensive use in applications ranging from the basic household utensils and general constructions to the high-end space vehicles and nuclear plants [1]. Cr is responsible for this “stainless” feature by forming a protective layer of Cr oxide on the surface. The amount of Cr should be above 11 wt.% at least [2], and normally more Cr is needed in severe environments. Stainless steels can be divided into four categories, based on their microstructure at room temperature: ferritic, martensitic, duplex (austenitic and ferritic) and austenitic stainless steels. A fifth grade is the precipitation-hardening stainless steels, in which the matrix is often martensitic [3]. The division of grades according to their microstructure is natural, considering the general differences in corrosion resistance and mechanical properties between the categories. This thesis will be focusing on austenitic and duplex stainless steels.

Austenitic stainless steels are the largest group and only grades 304/304L account for about 50% of the global production of stainless steels [3]. They have good creep resistance, toughness, ductility, weldability and corrosion resistance. However, austenitic stainless steels are usually susceptible to stress corrosion cracking due to intergranular internal oxidation [4]. Duplex stainless steels, with alternating ferrite (hereinafter referred to as

$\alpha$ ) and austenite (hereinafter referred to as  $\gamma$ ) structures, provide high strength as well as high resistance to stress corrosion cracking [5].

Recently, a research focus is on the improvement of mechanical properties of austenitic and duplex stainless steels, for example, on the increase of strength without significant ductility/formability loss [5,6]. The  $\gamma$  stability has been tailored for this purpose to make use of the deformation-induced martensitic transformation (DIMIT). This gives rise to a delayed necking, which is usually termed transformation-induced plasticity (TRIP) effect. To date, the TRIP effect has become quite popular in the steel industry [7] and, for example, it is exploited in the development of 3<sup>rd</sup> generation high strength steels [8–10]. Hence, the understanding of controlling factors of  $\gamma$  stability, deformation mechanism and related micromechanics of constituent phases is important for tailoring the mechanical properties of alloys with TRIP effect.

## 1.1 Scope of present work

In view of the complicated mechanism of DIMIT, our work started from Fe-Cr-Ni metastable austenitic model alloys for a better understanding of nucleation sites, transformation routes and deformation microstructure correlated with stacking fault energy (SFE). Part of this work has been dedicated to the comparison between athermal and deformation-induced martensite to find the controlling factors for martensite formation. Special attention has been paid to the roles of  $\epsilon$ -martensite (hereinafter referred to as  $\epsilon$ ) and other related planar defects on the martensitic transformation. Moreover, the work has also extended to investigating the micromechanics of defects and constituent phases in TRIP-assisted duplex stainless steels (TDSS) with the knowledge gained from model alloys. Special attention is also being given to the dependence of DIMIT on the orientation.

Electron channeling contrast imaging and electron backscatter diffraction in scanning electron microscopy were applied for defect characterization. High-energy X-ray diffraction was used for *in situ* studies of phase fraction evolution and stress partitioning during loading. In addition, the individual

grains were tracked and analyzed using three-dimensional X-ray diffraction with *in situ* cooling environment.



## 2 DEFORMATION BEHAVIOR OF TRIP-ASSISTED STAINLESS STEELS

The deformation behavior of polycrystalline materials is more complicated than single crystalline materials due to the interactions between adjacent grains with different or similar orientations [11]. TRIP-assisted stainless steel is a kind of polycrystalline material that makes use of the metastable phase ( $\gamma$ ) which can be transformed into  $\alpha'$ -martensite (hereinafter referred to as  $\alpha'$ ) during deformation. This transformation has a large influence on the plastic flow which leads to a ductility enhancement [12,13].

The understanding of the ductility enhancement due to the TRIP effect has been investigated extensively [14–16]. Bhadeshia [17] investigated the ductility contribution from transformation strain perspective only. It was found that the contribution is maximum 15% for fully austenitic steels that are transformed completely to martensite, whereas the contribution in multiphase alloys must consider the initial  $\gamma$  volume fraction and the extent of transformation. Thus, this contribution is rather small compared with the total ductility enhancement. Greenwood & Johnson [18] and Zackay [19] argued that the extra work hardening due to the phase transformation can stabilize the plastic flow confined to the weaker phase, which gives rise to a delayed necking. Jacques *et al.* [20] further attributed the superior uniform elongation to a so-called composite strengthening effect, in which the deformation-induced  $\alpha'$  strengthens the matrix and provides a sort of “shielding” effect indirectly stabilizing the adjacent metastable  $\gamma$ .

## 2.1 Deformation in austenitic stainless steels

Generally, stable austenitic stainless steels with a face-centered cubic (*fcc*) structure deform via slip on the close-packed  $\{111\}\gamma$  planes along  $\langle 110 \rangle$  directions. The activation of specific slip system within a grain depends on the relationship between critical resolved shear stress and the actual resolved shear stress. If a slip system is activated, the actual resolved shear stress must be higher than the critical resolved shear stress. The actual resolved shear stress can be estimated based on the Schmid's law [21]. For uniaxial tensile loading, the resolved shear stress along the slip direction can be described as shown in Fig. 2.1 where:

$$\tau_{RSS} = \sigma \cdot \cos \lambda \cdot \cos \varphi = \sigma \cdot m \quad (1)$$

where  $\sigma$  is the applied tensile stress;  $\lambda$  is the angle between tensile direction and slip direction;  $\varphi$  is the angle between the tensile direction and slip plane normal;  $\cos \lambda \cdot \cos \varphi$  is the Schmid factor which is usually termed  $m$ .

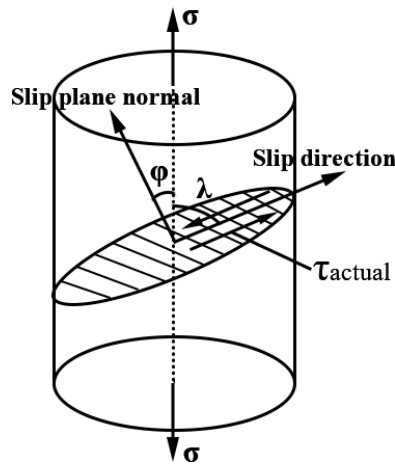


Fig. 2.1 Schematic diagram of the relationship between the applied stress and resolved shear stress on a slip direction.

In metastable austenitic stainless steels, another deformation mechanism is observed with a slip system of  $\{111\}\langle 112 \rangle$  [22]. In such case, a perfect dislocation may dissociate into two Shockley partial dislocations, and

therefore, an intrinsic stacking fault can be observed between two partials. The different arrangements of stacking faults result in the formation of  $\epsilon$  or mechanical twins depending on the SFE [23–25]. Remy and Pineau [26] discussed the effect of SFE on the deformation mechanisms. The formation of  $\epsilon$  with CACACA stacking (hexagonal close-packed, *hcp*) is preferred at SFEs less than about  $10 \text{ mJ m}^{-2}$  [23]. When SFE increases, the  $\epsilon$  formation is restricted, and consequently, the mechanical twinning becomes the main deformation mechanism with the arrangement of stacking faults on every consecutive layer of  $\{111\}\gamma$ . The irregularly overlapped stacking faults,  $\epsilon$  and mechanical twins are normally collectively termed shear bands [27], which is the main deformation characteristic in metastable austenitic stainless steels. In addition, another deformation feature,  $\alpha'$ , has been observed at both individual shear bands [28] and the intersections [29] giving a large influence on the micromechanics during deformation.

## 2.2 Deformation in multiphase stainless steels

For decades, efforts have been made to improve the mechanical properties of multiphase stainless steels by making use of the hard constituents such as  $\alpha'$  [5,30,31]. The continuous formation of the harder  $\alpha'$  within  $\gamma$  gives rise to a load redistribution between the constituent phases, which is quite different than normal plastic deformation in single-phase austenitic steels. According to Bao *et al.* [32], small hard constituent like  $\alpha'$ , act as precipitates, and can introduce a precipitation-hardening effect for the matrix. With high volume fraction of  $\alpha'$ , a continuous network of  $\alpha'$  called “percolating cluster” forms [33] and influences the plastic flow of the materials during the deformation. This leads to the “shielding” effect for nearby  $\gamma$ . In addition, the change in relative strength of constituent phases could lead to a different load partitioning as well. For example, the solid-solution strengthening of  $\alpha$  could lead to an indirect stabilization of the metastable  $\gamma$  with less load partitioned via the composite strengthening effect [20].

## 2.3 Deformation-induced martensitic transformation (DIMIT)

### 2.3.1 Martensite formation and related crystallography

Martensitic transformation involves a Bain distortion and a transformation shear according to the phenomenological theory. The transformation could also be characterized as diffusionless and displacive with a special habit plane, *i.e.* invariant plane. Two main types of morphology have been observed in ferrous  $\alpha'$ , *i.e.* lath and plate  $\alpha'$  [34]. Much focus has been paid to the lath  $\alpha'$  due to its existence in most commercial steels, *e.g.* in the studied stainless steels [35].

The  $\alpha'$  variants are crystallographically equivalent with special orientation relationships (OR) to the prior  $\gamma$  grains. The special OR is commonly the Kurdjumov-Sachs orientation relationship (KS-OR) ( $\{111\}\gamma//\{011\}\alpha'$ ,  $\langle 110\rangle\gamma//\langle 111\rangle\alpha'$ ), and it was first discovered in a 1.4 wt.% C steel using X-rays. Another common OR is called Nishiyama-Wasserman orientation relationship (NW-OR) ( $\{111\}\gamma//\{011\}\alpha'$ ,  $\langle 112\rangle\gamma//\langle 011\rangle\alpha'$ ), which was found in a Fe-30%Ni alloys. NW-OR and KS-OR deviate from each other by about  $5^\circ$  [36]. According to the nomenclature of Morito *et al.* [34], the KS-OR with 24 variants could be defined as V1-V24 as shown in Table 2.1. Therefore, it is reasonable to expect that selected  $\alpha'$  variants will form preferentially in response to the stress or strain field during deformation. This variant selection behavior has been observed by many researchers [37–39].

An attempt to correlate this variant selection behavior with the double shear mechanism was made by Higo *et al.* [40]. Olson and Cohen [41] summarized the double shears (two invariant-plane strains) as one-third *fcc* twinning shear and one-half *fcc* twinning shear. Hence, the formation of  $\alpha'$  is triggered when the first shear plane intersects with the second shear plane. From the invariant plane, a given pair of the shears could be easily associated with the specific KS-OR variant. Using the notation of the Thompson's tetrahedron as shown in Fig. 2.2, the correlation between

double shear processes and 24 KS-OR variants is shown in Table 2.1 [34,40,42]. Since  $\alpha'$  was found to nucleate at the intersection of shear bands as well as individual shear bands [28,43], the double shears can be extended to a more general form which is discussed in Paper III. Moreover, the selective behavior may be influenced by the special local stress field within the shear regions as well [44].

Table 2.1 24 KS-OR variants in relation to the double shear mechanism.

Variant notation	Parallel plane ( $\gamma$ )//( $\alpha'$ )	KS-OR		Double shear processes (Bogers-Burgers)	
		Parallel direction [ $\gamma$ ]// [ $\alpha'$ ]		1 <sup>st</sup> shear	2 <sup>nd</sup> shear
V1	(111)//(011)	[ -1 0 1 ]	]/]/[ -1 -1 1 ]	B $\delta$	C $\alpha$
V2		[ -1 0 1 ]	]/]/[ -1 1 -1 ]	C $\delta$	B $\alpha$
V3		[ 0 1 -1 ]	]/]/[ -1 -1 1 ]	C $\delta$	A $\beta$
V4		[ 0 1 -1 ]	]/]/[ -1 1 -1 ]	A $\delta$	C $\beta$
V5		[ 1 -1 0 ]	]/]/[ -1 -1 1 ]	A $\delta$	B $\gamma$
V6		[ 1 -1 0 ]	]/]/[ -1 1 -1 ]	B $\delta$	A $\gamma$
V7	(1-11)//(011)	[ 1 0 -1 ]	]/]/[ -1 -1 1 ]	C $\alpha$	B $\delta$
V8		[ 1 0 -1 ]	]/]/[ -1 1 -1 ]	B $\alpha$	C $\delta$
V9		[ -1 -1 0 ]	]/]/[ -1 -1 1 ]	D $\alpha$	C $\beta$
V10		[ -1 -1 0 ]	]/]/[ -1 1 -1 ]	C $\alpha$	D $\beta$
V11		[ 0 1 1 ]	]/]/[ -1 -1 1 ]	B $\alpha$	D $\delta$
V12		[ 0 1 1 ]	]/]/[ -1 1 -1 ]	D $\alpha$	B $\gamma$
V13	(-111)//(011)	[ 0 -1 1 ]	]/]/[ -1 -1 1 ]	A $\beta$	C $\delta$
V14		[ 0 -1 1 ]	]/]/[ -1 1 -1 ]	C $\beta$	A $\delta$
V15		[ -1 0 -1 ]	]/]/[ -1 -1 1 ]	D $\beta$	A $\delta$
V16		[ -1 0 -1 ]	]/]/[ -1 1 -1 ]	A $\beta$	D $\delta$
V17		[ 1 1 0 ]	]/]/[ -1 -1 1 ]	C $\beta$	D $\alpha$
V18		[ 1 1 0 ]	]/]/[ -1 1 -1 ]	D $\beta$	C $\alpha$
V19	(11-1)//(011)	[ -1 1 0 ]	]/]/[ -1 -1 1 ]	B $\gamma$	A $\delta$
V20		[ -1 1 0 ]	]/]/[ -1 1 -1 ]	A $\gamma$	B $\delta$
V21		[ 0 -1 -1 ]	]/]/[ -1 -1 1 ]	D $\gamma$	A $\alpha$
V22		[ 0 -1 -1 ]	]/]/[ -1 1 -1 ]	B $\gamma$	D $\alpha$
V23		[ 1 0 1 ]	]/]/[ -1 -1 1 ]	A $\gamma$	D $\beta$
V24		[ 1 0 1 ]	]/]/[ -1 1 -1 ]	D $\gamma$	A $\beta$

\*The shear is represented by Thompson's tetrahedron notation as shown in Fig. 2.2.

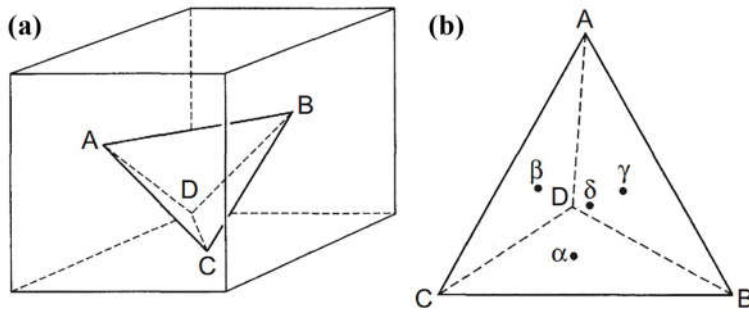


Fig. 2.2 Schematic diagram of Thompson's tetrahedron notation [45].

### 2.3.2 Thermodynamics and kinetics

The formation of athermal  $\alpha'$  takes place at the martensite start temperature ( $M_s$ ), where the chemical driving force  $\Delta G^{\gamma \rightarrow \alpha'}$  reaches the critical value to overcome an energy barrier. However, the martensitic transformation can be triggered by deformation just above  $M_s$  with an extra mechanical driving force. Patel and Cohen [46] suggested that the mechanical driving force from the applied stress can be described as follows:

$$U = \tau \cdot \gamma_0 + \sigma \cdot \varepsilon_0 \quad (2)$$

where  $\tau$  and  $\sigma$  represent the shear and normal stresses,  $\gamma_0$  and  $\varepsilon_0$  are the shear strain and the normal strain respectively. Suzuki *et al.* [47] claimed that the formation of  $\alpha'$  could not only be attributed to the applied stress, instead the internal stresses within dislocation pile-ups provide additional mechanical driving force when there is plastic deformation. In Fig. 2.3a, the schematic plot of chemical free energy against temperature for  $\gamma$  and  $\alpha'$  is shown and the required mechanical driving force at  $T_1$  is presented as an example. It should be noted that the required mechanical driving force for martensitic transformation depends on the temperature as well as the alloy composition.

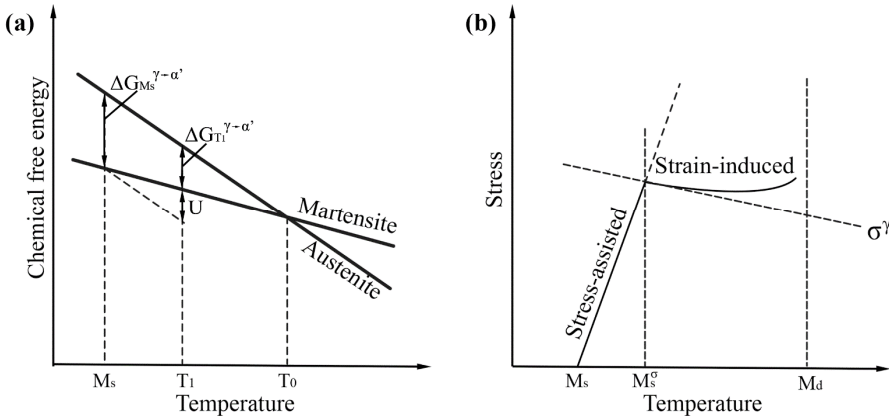


Fig. 2.3 Schematic plot of (a) chemical free energy against temperature for  $\gamma$  and  $\alpha'$  [48]; and (b) related stress and temperature effect on DIMT [41].

DIMT can be defined as stress-assisted or strain-induced according to the nomenclature introduced by Olson and Cohen, see schematic plot in Fig. 2.3b [41]. The boundary temperature between the two regions was first defined as  $M_s^\sigma$  by Richman and Bolling [49]. In the stress-assisted region,  $\alpha'$  nucleates on the same sites as athermal  $\alpha'$  but assisted by applied stress. While in strain-induced region,  $\alpha'$  forms near the defects produced by plastic deformation. When the temperature is above the  $M_d$  temperature, martensitic transformation cannot be triggered by deformation anymore.

Based on the double shear mechanism, the transformation kinetics of strain-induced martensitic transformation was described by Olson and Cohen [50]. The description considered the shear-band formation, shear-band intersection and the probability of  $\alpha'$  nucleation at the intersections of shear bands, and it further modeled the  $\alpha'$  volume fraction ( $f^{\alpha'}$ ) as a function of plastic strain ( $\varepsilon'$ ) as follows:

$$f^{\alpha'} = 1 - \exp\{-\beta[1 - \exp(-\alpha'' \cdot \varepsilon')]^n\} \quad (3)$$

where  $\beta$  and  $\alpha''$  are temperature-dependent parameters, and  $n$  is a fixed exponent.  $\beta$  is proportional to the probability of  $\alpha'$  nucleation at the intersections of shear bands.  $\alpha''$  depends on the SFE. The value of  $n$  was found to be about 4.5 for 304 stainless steels. Fig. 2.4 shows a comparison

of this model with experimental data of 304 stainless steels. Good agreements were achieved and a strong temperature dependence of the DIMT was revealed. The predicted curves follow a sigmoidal manner in the strain-induced regime, while curves of stress-assisted martensitic transformation were reported to be almost linear [47].

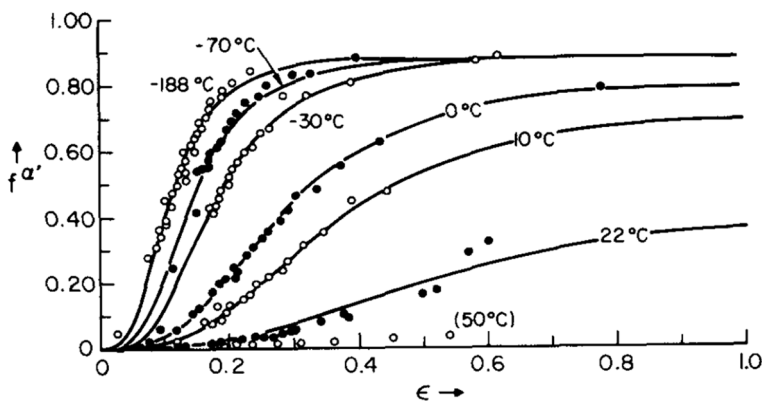


Fig. 2.4 The illustration of comparison between modeled kinetic curves and experimental datasets over several temperatures for 304 stainless steels [50].

### 2.3.3 Stacking fault energy

In addition to chemical driving force, the nucleation and growth of  $\alpha'$  can also be associated with the formation of shear bands [51], which is largely influenced by SFE as mentioned in section 2.1. It has been observed that the existence of shear bands consisting of  $\epsilon$  could reduce the activation energy for the  $\alpha'$  formation [24]. Therefore, it is natural to expect that the formation of shear bands is important to facilitate the formation of  $\alpha'$ . Sato *et al.* [52] suggested that the pre-existing  $\epsilon$  could facilitate the formation of  $\alpha'$  even above  $M_d$ , while the pre-existing shear bands without  $\epsilon$  couldn't trigger the formation of  $\alpha'$ . It should be noted that severe localized strain could also facilitate the  $\alpha'$  formation by the accommodation of many dislocations [53]. In view of the crucial effect of SFE on the formation of shear bands, efforts have been made to measure SFE experimentally and to estimate SFE theoretically. SFE could be obtained using transmission electron microscopy based on dislocation node observations [54], and X-

ray diffraction (XRD) based on X-ray line broadening analysis and stacking fault probability determination [55].

Many empirical equations for estimating SFE are also available. In our preliminary work [56], a formula proposed by Schramm and Reed was used to estimate SFEs for a series Fe-Cr-Ni model alloys. However, the result was not satisfactory. There are also theoretical works available for the SFE determination. In Paper II, the SFEs of Fe-Cr-Ni model alloys were calculated using first-principles based on axial next-nearest-neighbor Ising model. Reasonable results were achieved. In Paper V, the trend of SFEs of  $\gamma$  within different TDSS was estimated thermodynamically [57] by calculating the molar Gibbs energy differences between  $\gamma$  and  $\epsilon$  ( $\Delta G^{fcc \rightarrow hcp}$ ) using Thermo-Calc [58].

### 2.3.4 Factors affecting deformation-induced martensitic transformation

The mechanical stability of  $\gamma$  reveals the tendency for  $\gamma$  to be transformed into  $\alpha'$  during deformation. It can be represented by the  $M_{d30}$  temperature, where 50%  $\gamma$  is transformed into  $\alpha'$  at 0.3 true strain.

The mechanical stability of  $\gamma$  could be affected by the variation of chemical composition. Lo *et al.* reported [2] that all alloying elements have effects on both the chemical driving force  $\Delta G^{\gamma \rightarrow \alpha'}$  and the SFE which are important for DIMT, however, inconsistencies exist for the same alloying element as well. The mechanical stability of  $\gamma$  can be additionally influenced by the temperature, since temperature also has an effect on both  $\Delta G^{\gamma \rightarrow \alpha'}$  and SFE. The deformation mechanism changes from shear banding to dislocation glide as the temperature increases, while the formation of  $\alpha'$  is restricted [59]. The effect of strain rate on the DIMT has mainly been attributed to the adiabatic heating [60]. In addition, the high strain rate could facilitate the formation of irregular shear bands consisting of less preferred nucleation sites for  $\alpha'$  formation [44].

The mechanical stability of  $\gamma$  might also be affected by the grain size. Nohara *et al.* [61] illustrated that the refinement of grain size could

stabilize the  $\gamma$ , and they proposed an empirical model to estimate the  $M_{d30}$  taking  $\gamma$  grain sizes into account. However, Matsuoka *et al.* [62] recently found that the influence of the  $\gamma$  grain size on DIMT in a metastable austenitic stainless steel is negligible. The grain size effect mainly affects athermal martensitic transformation, especially below 20  $\mu\text{m}$ , due to the spatial restriction effect.

# 3 EXPERIMENTAL METHODS

## 3.1 Materials and sample preparations

Fe-Cr-Ni austenitic model alloys and commercial TDSS were investigated in this work. Both lab-scale and industrial-scale methods were used for the preparation of Fe-Cr-Ni model alloys. Paper I-III were based on the model alloys produced by lab-scale arc-melting. Part of Paper I was additionally supported by model alloys fabricated by industrial-scale melting. Paper IV and Paper V were based on commercial TDSS from Outokumpu Stainless.

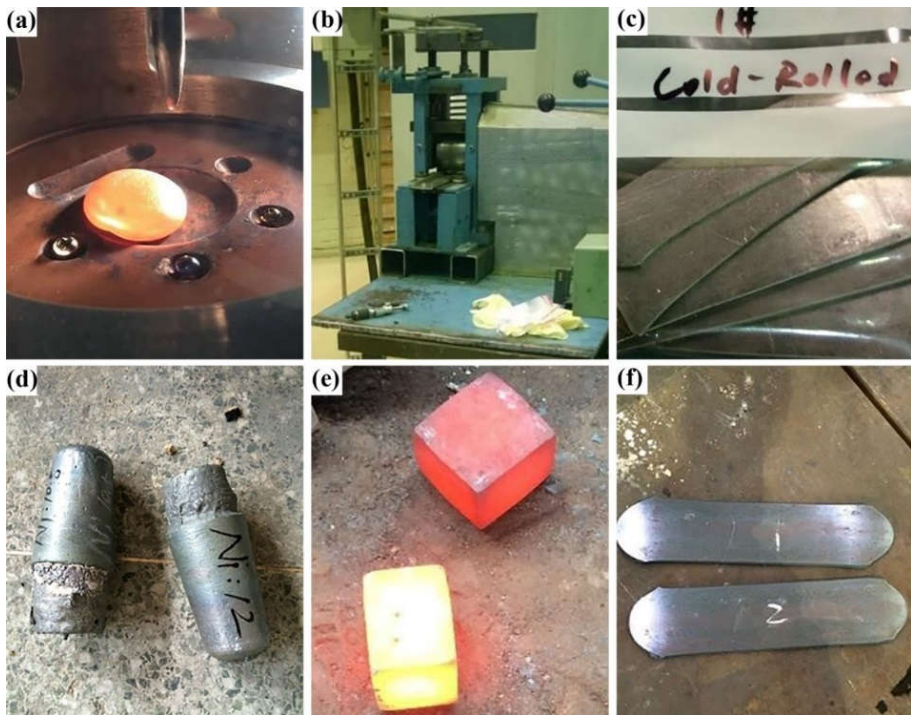


*Fig. 3.1 The illustration of alloy preparation for model alloys, (a) arc-melting, (b) cold rolling, (c) sheet-like samples after cold rolling, (d) industrial-scale casted samples, (e) hot forged samples, (f) hot rolled samples.*

The detailed procedure of the sample preparation is shown in Fig. 3.1. The lab-scale samples were produced using a compact arc-melter, and button-shaped samples were obtained as shown in Fig. 3.1a. Compression and high temperature annealing at 1200 °C were performed to obtain a homogeneous structure with negligible segregations. Cold rolling was then carried out to have sheet-like samples with a thickness of 2 mm using a small cold roller as shown in Fig. 3.1b. The final products are as shown in Fig. 3.1c, and these sheet-like samples were further annealed for the following deformation studies. The large samples, as shown in Fig. 3.1d, were produced using vacuum induction melting followed by hot forging (Fig. 3.1e). Then the cube samples were hot rolled into sheet-like samples as shown in Fig. 3.1f. Further cold rolling and annealing were also performed for different purposes.

In Paper I, bar-shaped samples with dimensions of  $1 \times 1 \times 15 \text{ mm}^3$  were prepared for *in situ* cooling experiments at the beamline P07 of PETRA III, DESY. In Paper II-III, the deformation was carried out using the small cold roller mentioned above. In Paper IV and Paper V, the samples for *in situ* loading experiment at the F2 beamline of CHESS were first designed using AutoCAD and the finite element method for determining suitable dimensions. They were then fabricated using electrical discharge machining. The dimensions of the dog-bone-shaped sample are as shown in Fig. 3.2a and b. A special sample holder was prepared (Fig. 3.2c) for mounting the sheet-like samples to the rotational and axial motion system [63].

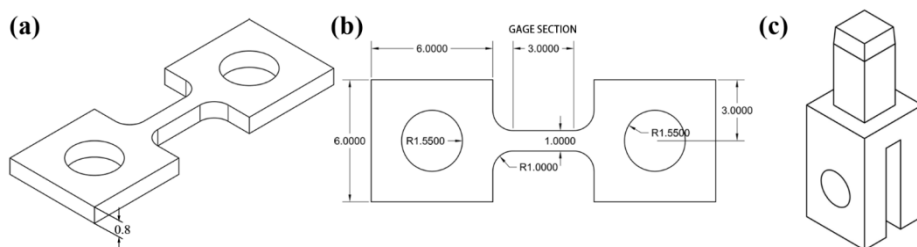


Fig. 3.2 The sample design for the *in situ* loading experiment at the F2 beamline of CHESS (All dimensions are in mm).

## 3.2 Microstructural characterization

### 3.2.1 Light optical microscopy (LOM)

Light optical microscopy (LOM) is a useful and convenient technique to acquire general microstructure information after sample preparation with the help of proper etchants. It can also assist the searching for areas of interest for further electron microscopic investigations. For example, deformation microstructures could be investigated using LOM. The planar defects and  $\alpha'$  could be etched dark as shown in Fig. 3.3. However, the detailed structure of them is beyond the resolution limit of LOM.

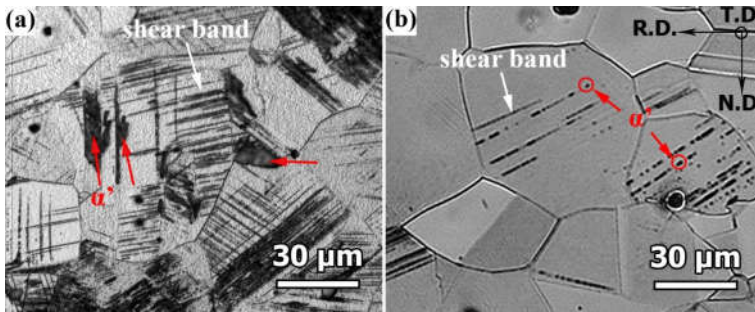


Fig. 3.3 LOM images of deformation microstructure of (a) Fe-18Cr-10Ni and (b) Fe-18Cr-11.5Ni alloys with 10% cold rolled reduction.

### 3.2.2 Scanning electron microscopy (SEM)

Scanning electron microscopy (SEM) is widely used for microstructure characterization, it gives much larger depth of field compared with LOM. SEM with a field emission gun (FE-SEM) enables high resolution characterization with excellent statistics. An electron beam scans the sample surface to generate different types of signals. The schematic diagram of interaction volume and related signals is shown in Fig. 3.4a. In the interaction between the incident beam and the surface of the sample, the secondary electrons, backscattered electrons and characteristic X-rays are the three main signals. The secondary electrons give us the topographical information of the sample surface; the backscattered electrons are sensitive to atomic number, orientation and phase differences; the characteristic X-rays can be used to measure the composition of

specific areas. However, the results are interaction volume dependent which are associated with the beam voltage and current [64]. In Paper IV, an attempt was made for the chemical composition analysis of constituent phases in TDSS using energy dispersive spectroscopy (EDS) in SEM based on the characteristic X-rays. The results were quite inaccurate due to the overlapping grains in the interaction volume. Therefore, transmission electron microscopy (TEM) was used to avoid this problem with much smaller interaction volume as shown in Fig. 3.4b.

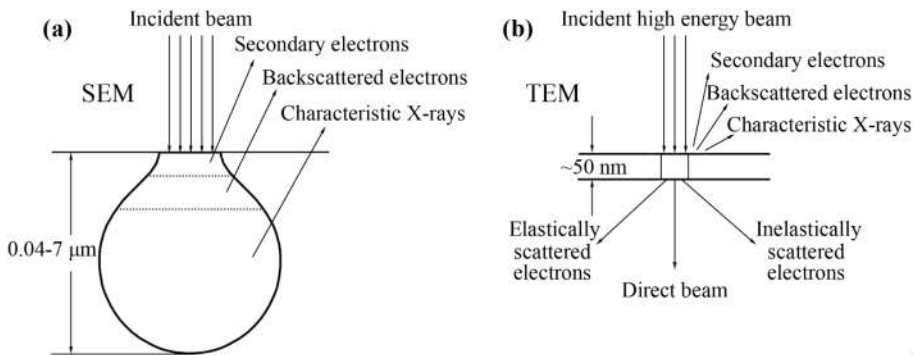
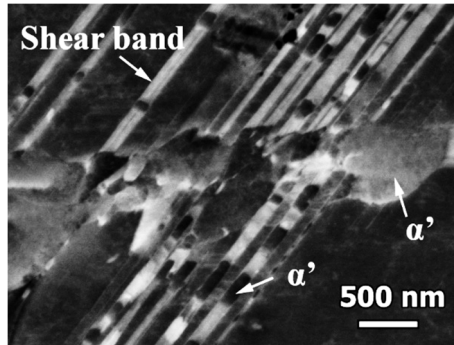


Fig. 3.4 Schematic diagrams of the interaction volume and generated signals in (a) SEM and (b) TEM [65].

### 3.2.2.1 Electron channeling contrast imaging (ECCI)

Electron channeling contrast imaging (ECCI) technique in SEM is based on the channeling effect of electrons and makes use of signals from the backscattered electrons. ECCI has enabled the characterization of crystal defects such as dislocations, planar defects and grain boundaries [66,67]. A grain with an orientation fulfilling Bragg condition with the incident beam would appear dark due to the much less backscattered signals. In distorted areas like defects, the Bragg condition will not be satisfied and therefore strong backscattering occurs. Hence, the defects will appear bright in the dark matrix. In addition, ECCI is quite sensitive to the orientation difference providing a good supplement to other techniques. In Paper II-IV, the ECCI technique was used to characterize the deformation microstructure as well as the crystallographic features of  $\alpha'$ . In Fig. 3.5,

the deformation structure of Fe-18Cr-10Ni model alloy with 10% cold rolled reduction is shown. The shear bands and  $\alpha'$  are clearly revealed.



*Fig. 3.5 The deformation structure of Fe-18Cr-10Ni model alloy with 10% cold rolled reduction.*

### 3.2.2.2 Electron backscatter diffraction (EBSD)

Electron backscatter diffraction (EBSD) is a SEM-based technique, which allows us to characterize the crystallographic features by analyzing the Kikuchi diffraction patterns as shown in Fig. 3.6a. Even though, Kikuchi patterns in TEM were first observed by Nishikawa and Kikuchi in 1928, the fast development of EBSD in SEM with automation mainly took place after 1990s [68]. The typical geometry of EBSD is illustrated in Fig. 3.6b. The incident beam firstly interacts with the sample surface producing some inelastically scattered electrons, and the subsequent elastic scattering satisfying Bragg's law projects a pattern onto the phosphor screen. This pattern is usually called electron backscatter diffraction pattern, which can be used to define the crystallographic information of the sample surface by matching with simulated patterns. The sample is usually tilted to 70°.

The pattern quality is largely affected by deformation. Hence, the deformation layer introduced from mechanical grinding/polishing has to be fully removed by careful ion-polishing or electrolytic polishing. For the investigation of DIMT, the sample preparation is important due to the easily introduced martensite with mild mechanical polishing or even during ion-polishing [69]. In the current study, the combination of mild

mechanical grinding and electrolytic polishing was used and further checked using LOM. The martensite introduced during the mechanical grinding normally appears in parallel with the grinding direction and the volume fraction of it varies depending on the grinding force and the parameters of electrolytic polishing.

EBSD was extensively used in the current work. In Paper I, it was used for the orientation relationship determination between constituent phases. In Paper II, it was used to identify individual phases. In Paper III, the  $\alpha'$  variant pairing tendency and variant selection behavior were observed and analyzed with it. In Paper IV, the local strain was estimated, and  $\alpha'$  and  $\alpha$  (both are body-centered cubic) were further separated based on mainly the pattern quality. In Paper V, the orientation dependence of  $\gamma$  stability was studied based on the Schmid's law and double shear mechanism with the help of EBSD.

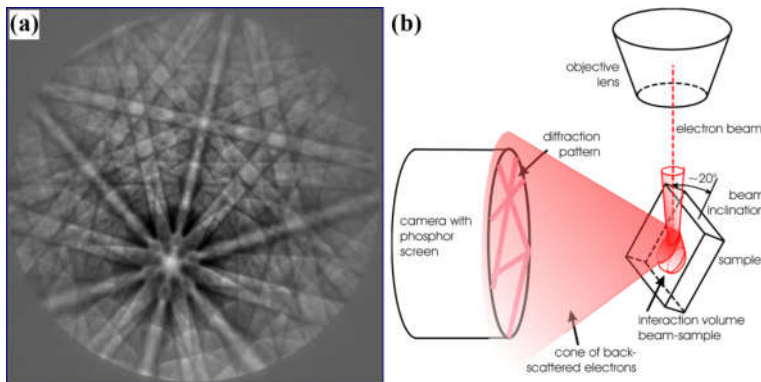


Fig. 3.6 (a) Diffraction pattern of Nb and (b) sketch of the geometry of EBSD in SEM [70].

### 3.2.2.3 EBSD data analysis using MTEX

MTEX is a free and open-source MATLAB toolbox for analyzing EBSD and XRD datasets in terms of orientation, texture, and plastic and elastic properties with no extra packages required. It is a versatile tool with automation and it can work with other software cooperatively [71].

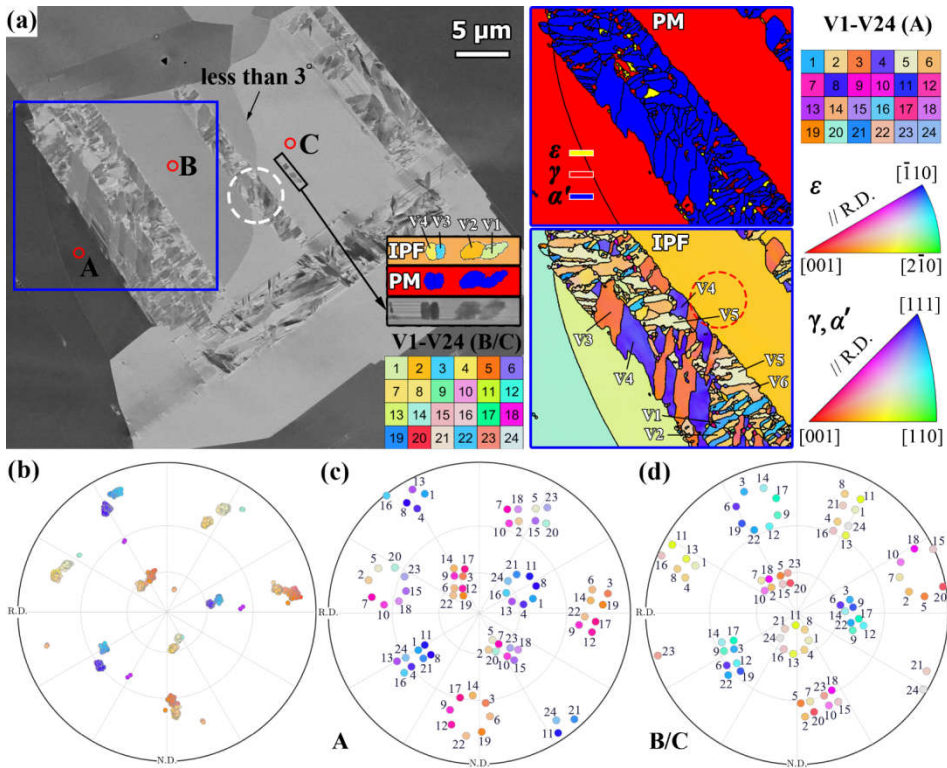


Fig. 3.7 Athermal martensite microstructure of Fe-18Cr-12Ni quenched to  $-196^{\circ}\text{C}$ : (a) ECCI and EBSD maps,  $[100]\alpha'$  stereographic projections for (b) the variants formed in the selected blue rectangular area and all possible 24 variants for parent  $\gamma$  with respect to (c) area A and (d) area B/C (the misorientation is within the symbols).

Advanced and automatic post-processing could be performed using MTEX [72]. In Paper III, for example, the variant pairing tendency for athermal martensitic transformation in alloy 18-12 could be analyzed as shown in Fig. 3.7.

### 3.2.2.4 Focused ion beam (FIB)

Focused ion beam (FIB) is a site-specific technique widely used in material science. Unlike SEM, FIB uses focused ions instead of electrons to image the sample and mill the sample. A Gallium ion source is commonly used due to its low melting point, no overlapping peaks in EDS spectrum, high beam intensity, low volatility, long life time, *etc.* Platinum is usually used

for deposition to protect the surface of the sample during milling [4]. A FEI Nova 600 FE-SEM equipped with FIB was used for the preparation of TEM samples in this work.

### **3.3 High-energy X-ray Diffraction (HEXRD)**

#### **3.3.1 Synchrotron radiation**

Synchrotron radiation is a kind of electromagnetic radiation which takes place when the high energy electrons are forced to accelerate perpendicular to their velocity. The radiation occurs along the tangential direction due to the change of velocity. The synchrotron X-ray was first discovered on a 70 MeV synchrotron facility at General Electric in 1947 [73]. However, it didn't become well-known as an important research tool until the 1960s since it was an undesirable effect in the beginning [74]. From the late 1980s, the demand of extremely bright X-rays propelled the development of synchrotron radiation leading to the construction of third-generation synchrotrons like ESRF, APS and Spring-8 [75]. To date, the synchrotron X-rays have become much more popular due to their high brilliance, which is more than a billion times higher than that of lab X-rays. This leads to a greater precision with more details for the material characterization. Moreover, the higher energy also gives rise to a larger penetration depth which enables the bulk analysis [76].

#### **3.3.2 *In situ* environment**

Recently, studies reveal a growing interest in synchrotron-based X-ray diffraction experiments during *in situ* tensile loading. It can be used to characterize texture evolution [13], phase fraction [10], micromechanics [77], martensite variant selection in the bulk of polycrystalline materials from sub-zero to elevated temperatures [10,78,79]. Torsional loading and complex loading could also be performed for similar types of analysis [80]. For example, Blondé *et al.* [81] investigated the stability of metastable  $\gamma$  in low-alloyed TRIP steel during shear loading and compared with normal tensile loading.

Apart from the deformation work, the temperature environment has been widely applied to the experiments at beamlines as well. Vandijk *et al.* [82] performed *in situ* cooling experiments to evaluate the thermal stability of retained  $\gamma$  in TRIP steels from grain-averaged perspective. Jimenez-Melero *et al.* [83] investigated the influence of Al and P on the thermal stability of individual  $\gamma$  grains in low-alloyed TRIP steels by cooling the alloys from room temperature down to  $-173$  °C.

Two *in situ* environments were used in the current study. In Paper I, an *in situ* cooling environment was used for the investigation of martensite formation in Fe-Cr-Ni model alloys. In Paper IV, the micromechanics and microstructure evolution of TDSS were studied during *in situ* uniaxial tensile loading.

### 3.3.3 Experimental setup

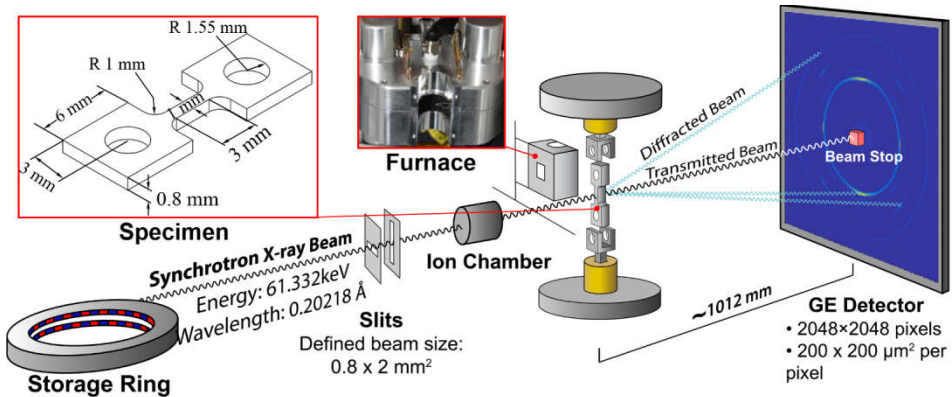


Fig. 3.8 Schematic illustration of the *in situ* X-ray diffraction study during tensile test with additional temperature environment, performed at CHESS, U.S.

Fig. 3.8 is an example of a setup in F2 beamline of CHESS. The X-rays are generated from the storage ring and further selected by a monochromator where the energy can be adjusted. The beam size is defined by a pair of slits perpendicular to each other. When X-ray irradiates the sample, the incident beam is diffracted into specific angles due to the lattice structure and interplanar spacing of the material.

### 3.3.4 Data analysis

The basic calibration and processing of the data could be performed using the GSAS-II software [84]. The 2D diffraction patterns as shown in Fig. 3.9a are integrated over 360° in the azimuthal direction ( $\eta$ ) to obtain the 1D profiles with grain-averaged information as shown in Fig. 3.9b. The 1D profiles can be fitted using the OriginLab software and a pseudo-Voigt function. In the current study, all peaks including low intensity  $\varepsilon$  peaks were fitted well using this procedure as shown in Fig. 3.9c.

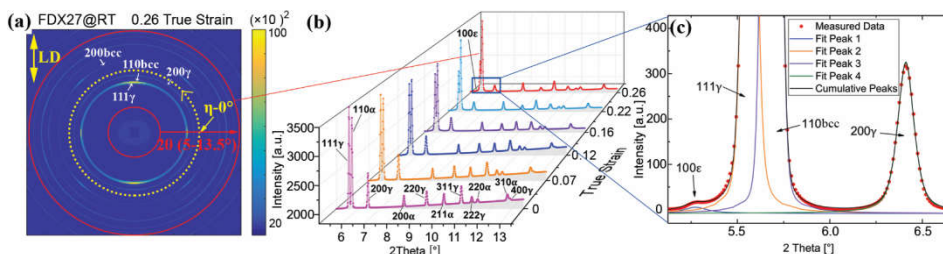


Fig. 3.9 Illustration of the data processing procedure for phase quantification, (a) 2D diffraction pattern of FDX27@RT at 0.26 true strain; (b) 1D diffraction profiles for different load conditions of FDX27@RT; (c) Goodness of fit for the indicated zoomed-in area of the 1D profile in (b), i.e. FDX27@RT deformed at 0.26 true strain.

#### 3.3.4.1 Volume fraction

The volume fractions of the constituent phases could be calculated using the direct comparison method [85]. This method is intended for powder diffraction analysis for random textures. The texture effect could be minimized by measuring multiple orientations and peaks for each phase [86]. The following equation can be used for the description of volume fraction:

$$V_i = \left( \frac{I}{n} \sum_{j=1}^n \frac{I_i^j}{R_i^j} \right) / \left( \frac{I}{p} \sum_{k=1}^p \frac{I_\gamma^k}{R_\gamma^k} + \frac{I}{q} \sum_{l=1}^q \frac{I_\varepsilon^l}{R_\varepsilon^l} + \frac{I}{r} \sum_{m=1}^r \frac{I_{bcc}^m}{R_{bcc}^m} \right) \quad (4)$$

where  $V_i$  is the volume fraction of phase- $i$ ;  $I_i^j$  ( $I_i^{hkl}$ ) is the integrated intensity for the  $\{hkl\}$  plane of phase- $i$ ;  $R_i^j$  ( $R_i^{hkl}$ ) is the scattering factor. Details can be found in Paper IV.

### 3.3.4.2 Lattice strain

The lattice strains along the tensile direction (integration over  $5^\circ$   $\eta$  sectors) could be measured based on the following equation:

$$\varepsilon_{hkl} = \frac{d_{hkl} - d_{hkl}^0}{d_{hkl}^0} \quad (5)$$

where  $d_{hkl}$  represents the measured lattice spacing at a given deformation, and  $d_{hkl}^0$  is the strain-free lattice spacing.

### 3.3.4.3 Stress partitioning between phases

The stress partitioning to a specific phase ( $\sigma_{phase}$ ) could be obtained by measuring  $d_{hkl}$  values and  $d_{hkl}$ -shifts accurately. Micro-mechanical models can be used to estimate the  $\sigma_{phase}$  values [87,88]. However, the accurate determination of  $d_{hkl}$ -shift in *fcc* alloys is challenging due to the contribution from the formation of stacking faults as shown in Fig. 3.10 [89].

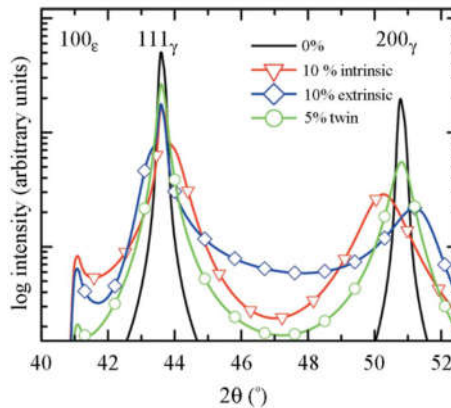


Fig. 3.10 Simulation results schematically showing the effect of stacking fault formation on the shift, broadening and asymmetry of diffraction peaks of  $\gamma$  [90].

Therefore, an alternative methodology could be applied. The MAUD software with Rietveld analysis can be used to refine the 2D diffraction patterns directly [91,92]. The  $\sigma_{phase}$ , root mean square (r.m.s.) microstrain, stacking fault probability, texture *etc.* can be obtained simultaneously from the refinement with the built-in models [88,93]. Fig. 3.11 shows an example of the measured and fitted diffraction patterns for FDX27@RT at 0.26 true strain obtained from MAUD. The details of individual models can be found in Paper IV.

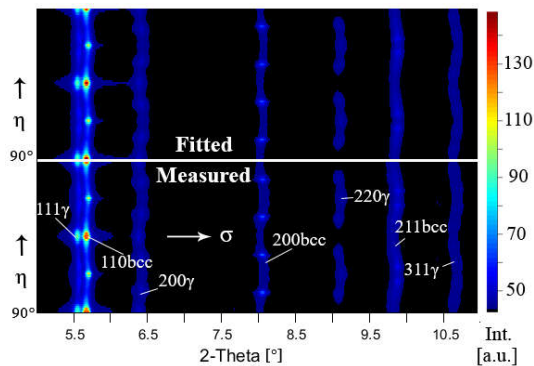


Fig. 3.11 2D representation of the diffraction data with 2-theta versus  $\eta$  and the color indicating the intensity of diffraction spots from black to red for specimen FDX27@RT at 0.26 true strain. (Top: Fitted results. Bottom: Measured results)

### 3.3.5 Three-dimensional X-ray diffraction (3DXRD)

Three-dimensional X-ray diffraction (3DXRD) is a promising method for the 3D mapping of individual grains within bulk materials in terms of center-of-mass position, orientation, lattice strain and even grain shape. It is a nondestructive method that enables even *in situ* investigations. This method usually makes use of high energy X-rays due to their high penetration power and short wavelength [94]. The experimental setup of 3DXRD is shown in Fig. 3.12. The idea is to acquire diffraction patterns for most of the grains within the intersected volume by rotating the sample along the vertical axis [94]. The diffraction patterns from a far-field detector (Fig. 3.12a) provide information of the grain position, orientation and strain with the help of a combination of FABLE and FitAllB packages

[95,96]. Then this information could be used as seeds for the following grain reconstruction using GrainSweeper.3d package, which is mainly based on the data acquired from a near-field detector as shown in Fig. 3.12b.

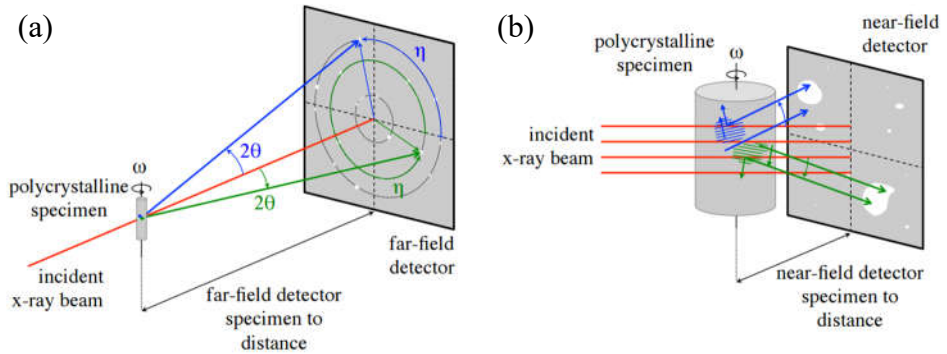


Fig. 3.12 The experimental setup of 3DXRD, (a) far-field diffraction, (b) near-field diffraction [97].

## *Experimental methods*

# 4 SUMMARY OF APPENDED PAPERS

## 4.1 Fe-Cr-Ni model alloys

### 4.1.1 Martensite formation during *in situ* cooling experiments (Paper I)

*In situ* grain-averaged and single-grain investigations of metastable austenitic Fe-18Cr-(10-11.5)Ni model alloys have been carried out during incremental cooling using HEXRD. The transformation sequence is found to be  $\gamma \rightarrow$  stacking faults  $\rightarrow \epsilon \rightarrow \alpha'$ , in which stacking faults act as precursors for  $\epsilon$  formation. The transient faulting is seen by the decrease of lattice d-spacing of  $\{222\}\gamma$  based on single-grain analysis. The role of  $\epsilon$  is crucial for the formation of  $\alpha'$  as observed from grain-average analysis due to the indistinguishable difference between  $M_s(\epsilon)$  and  $M_s(\alpha')$ . A parallel can be made to the deformation of low SFE alloys that the formation of potent defects is effective to facilitate DIMT. Fig. 4.1 is the graphical abstract of Paper I, which shows the setup of the *in situ* cooling experiment, the procedure of data analysis and the figure showing the collapse of lattice d-spacing of  $\{222\}\gamma$  together with the volume fraction evolution.

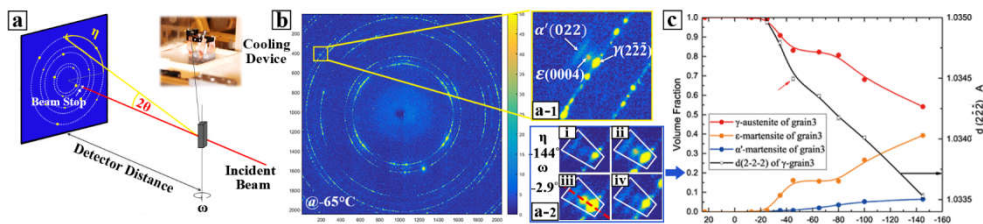


Fig. 4.1 The graphical abstract of Paper I, (a) the setup of *in situ* cooling experiment using HEXRD, (b) X-ray diffraction pattern of Fe-18Cr-10.5Ni at  $-65^\circ\text{C}$ , (c) Volume fraction evolution based on integrated area for an individual grain and the collapse of lattice d-spacing of  $\{222\}\gamma$ .

### 4.1.2 The deformation microstructure and deformation-induced martensite depending on SFE (Paper II)

The deformation microstructure of  $\gamma$  and the formation of martensite in Fe-18Cr-(10-12)Ni model alloys are characterized using ECCI and EBSD. They have been correlated to the Ni composition and SFE as summarized in Fig. 4.2. It was found that blocky  $\alpha'$  forms in between different sets of shear bands in unstable  $\gamma$  with quite low SFE ( $6.6 \text{ mJ m}^{-2}$ ). In this case, a lot of  $\alpha'$  units form within individual shear bands, and the intersections of shear bands are not the necessary precursors. For the more stable  $\gamma$  with larger SFE ( $9.6$  to  $9.8 \text{ mJ m}^{-2}$ ), the formation of mechanical twins is becoming thermodynamically preferred. Nucleation of  $\alpha'$  units within individual shear bands is less frequent, and the nucleation sites of  $\alpha'$  are usually adjacent to  $\varepsilon$ . The role of  $\varepsilon$  here has been attributed to reducing the activation energy for  $\alpha'$  nucleation. For the most stable  $\gamma$  with the highest SFE ( $12.4 \text{ mJ m}^{-2}$ ), only mechanical twins and irregular stacking faults are inside individual shear bands. The formation of  $\alpha'$  within this type of shear bands cannot be observed at the early stage of deformation. Further deformation is required to facilitate the  $\alpha'$  formation within highly distorted areas.

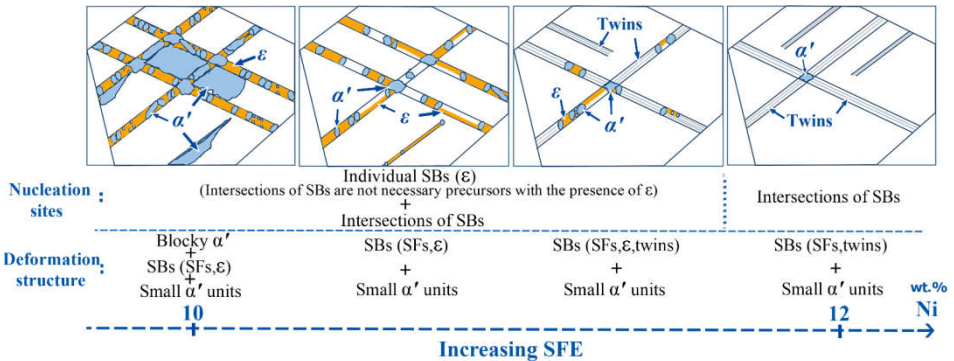


Fig. 4.2 The graphical abstract of Paper II showing the correlation between deformation microstructure and SFE in Fe-Cr-Ni alloys with Ni variation. SB: Shear band, SF: Stacking fault.

### 4.1.3 Comparing the deformation-induced martensitic transformation with the athermal martensitic transformation in Fe-Cr-Ni alloys (Paper III)

The microstructure and related crystallography of athermal and deformation-induced martensite in Fe-Cr-Ni alloys have been investigated. LOM, ECCI and EBSD were used for the characterization. The comparison between athermal and deformation-induced martensite with different  $\gamma$  stability leads to the new detailed correlation between deformation microstructure and SFE/ $\gamma$  stability as shown in Fig. 4.3. Two different types of structure are observed, *viz.* blocky and banded structure. The formation of blocky  $\alpha'$  takes places when the  $\gamma$  stability is low (stage 1 and 2); whereas the banded structure, consisting of shear bands and  $\alpha'$ , is related to the formation of  $\epsilon$  (stage 2 and 3). The formation of twin-related variants in deformed state could be attributed to the accommodation of the transformation shape strain. Hence, these variants will contribute little to the global plastic strain. Individual  $\alpha'$  variants form within individual shear bands adjacent to  $\epsilon$  when the stress condition is favorable, and therefore contribute to the global plastic strain. The Schmid's law and the double shear mechanism are found to be applicable to estimate the variant selection behavior. When the  $\gamma$  becomes less stable (stage 4), the  $\alpha'$  mainly forms at the intersections and can be additionally supported by surrounding dislocations (stage 5).

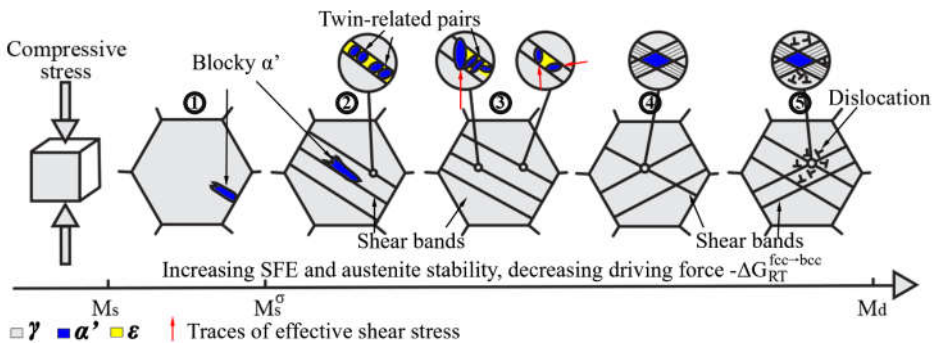


Fig. 4.3 The schematic diagram of the relationship between deformation microstructure and mechanical stability of  $\gamma$ .

## 4.2 TRIP-assisted duplex stainless steels

### 4.2.1 Micromechanics and microstructure evolution during *in situ* uniaxial tensile loading of TRIP-assisted duplex stainless steels (Paper IV)

Two TDSS, with three different stabilities of the  $\gamma$  phase, were investigated by HEXRD during *in situ* uniaxial tensile loading. The micromechanics and the DIMT in the bulk of the alloys were tracked and analyzed. Electron microscopy was used to supplement the HEXRD study providing the localized deformation structure analysis. The correlation between SFE and deformation structure assembles that of single-phase austenitic model alloys as described in Paper II. The blocky  $\alpha'$  is only frequent when the  $\gamma$  stability is low, and the formation of  $\alpha'$  comes together with the formation of shear bands. The formation of the microstructural features, *i.e.* defects and deformation-induced  $\alpha'$ , gives rise to additional influence on the initial load partitioning and following redistribution due to the elastoplastic anisotropy and martensitic transformation. The major redistribution takes place at the point where maximum martensitic transformation rate is reached. A clear work-hardening behavior is seen in the TDSS with the least stable  $\gamma$ .

#### **4.2.2 Mechanical stability of austenite grains towards martensitic transformation in a TRIP-assisted duplex stainless steel (Paper V)**

Slow uniaxial tensile loading experiment was carried out to investigate the mechanical behavior of  $\gamma$  in the TDSS, especially the orientation dependence of  $\gamma$  stability. The loading axis is parallel to the lamellas, *i.e.* rolling direction. The deformation microstructure was characterized using EBSD, and the orientation dependence was further analyzed based on the Schmid's law and double shear mechanism. It is found that  $\gamma$  grains, with multiple activated slip planes, typically transform preferentially at a certain applied stress. It can be attributed to the fact that more  $\alpha'$  variants could form due to the double shear mechanism, and therefore they can easily accommodate themselves to the global plastic strain.

*Summary of appended papers*

# 5 CONCLUDING REMARKS AND FUTURE WORK

## 5.1 Concluding remarks

This thesis aims to investigate the nature of DIMT in stainless steels. The focus is on: (1) The exploration of the state-of-the-art techniques that can be used for the characterization of deformation structures and deformation-induced martensite. (2) The microstructural investigation of Fe-Cr-Ni model alloys with different  $\gamma$  stabilities and SFEs. (3) The study of DIMT and related micromechanics of defects and constituent phases in TDSS.

From the systematic investigation of both model alloys and commercial grades, the main conclusions are as follows:

- ❖ The HEXRD is proven to be valuable for the characterization of micromechanics and structures. ECCI combined with EBSD is powerful for deformation structures and defect characterization.
- ❖  $\varepsilon$  is found to act as preferred nucleation sites for  $\alpha'$  from grain-average analysis, and a transient faulting state before  $\varepsilon$  formation is seen from single grain analysis. This indicates that the generation of potent nucleation sites is critical for deformation-induced  $\alpha'$  formation.
- ❖ The deformation microstructure of both Fe-Cr-Ni model alloys and TDSS can be correlated with SFE. The presence of  $\varepsilon$  makes the nucleation of  $\alpha'$  within individual shear bands possible. The appearance of blocky  $\alpha'$  at early stages of deformation indicates a rather unstable  $\gamma$  with low SFE.
- ❖ The formation of twin-related variants in deformed samples is similar to that in quenched samples, and it can be attributed to the accommodation behavior for the transformation shape strain.

Hence, these variants would contribute little to the global plastic strain. While individual  $\alpha'$  variants formed in a selective manner would influence the global plastic flow of the alloys. The formation of this variant selection could be rationalized by the Schmid's law and double shear mechanism.

- ❖ The microstructural features and the micromechanics of TDSS have been correlated with the  $\gamma$  stability. A pronounced TRIP effect with elastoplastic load transfer is observed in alloys with the least stable  $\gamma$ . The load transfer from the weaker phases to the stronger  $\alpha'$  takes place especially close to the point of maximum rate of  $\alpha'$  formation.
- ❖ The grain-orientation-dependent  $\gamma$  stability could be correlated to the number of active slip planes. The Schmid's law is proven to be useful to estimate the active slip planes. More active slip planes would facilitate the formation of more selective  $\alpha'$  variants which could easily accommodate themselves to the global plastic strain.

## **5.2 Future work**

In the present work, only the Ni content was tailored for the different  $\gamma$  stability/SFE of the model alloys in terms of the microstructure correlation and comparison. In fact, other contents, such as C, N, Mn, *etc.*, are also important from an industrial perspective, and the evaluation of the correlation between deformation structure and  $\gamma$  stability/SFE in general would be of great interest.

In the investigation of TDSS, the main focuses were the micromechanics and microstructure evolution with the variation of  $\gamma$  stability. However, grain sizes of constituent phases and the thermomechanical history are of great interest as the morphology and relative strength of the phases differ a lot.

The current study mainly focuses on the conventional microstructure characterization techniques like ECCI and EBSD. Information of localized areas around the defects and deformation-induced martensite is still

lacking. Although HEXRD, especially 3DXRD, has been used for the grain position, crystallography and stress/strain analysis. The information is still limited to a more averaged sense, *i.e.* over many grains (grain-averaged analysis) or a whole individual grain (single-grain analysis), instead of site-specific areas adjacent to defects. With the new development of transmission Kikuchi diffraction in SEM [98], the deformation microstructure could be investigated with much higher resolution for the site-specific areas prepared by FIB. Using high resolution EBSD [99], the localized stress/strain field could be measured and further compared with the simulation results based on crystal plasticity finite element method. Furthermore, *in situ* SEM measurements are desirable for an exhaustive study.

*Concluding remarks and future work*

# ACKNOWLEDGEMENTS

Firstly, I would like to express my sincere gratitude to my principle supervisor, assoc. Prof. Peter Hedström, who leads me into this exciting field and guides me with endless patience. I am also grateful for his understanding and straightforward communication between us.

Thanks also goes to my co-supervisor Prof. Annika Borgenstam, for her meaningful discussions and professional guidance, especially in revising the manuscripts. Many thanks to Prof. John Ågren for his support in the start of my Ph.D.

Further thanks go to my co-authors and collaborators, Oleg Gorbatov, Andrei Ruban, Ulrich Lienert, Jan Jonson, Torben Fischer, Peter Ko, Sen Lin, Yadunandan Das and Prasath Babu, for their help in my experiments. Over the past several years, I spent plenty of time in the laboratory, where Wenli Long gave a lot of support. Many thanks to her for the selfless dedication to my work.

Thank all the friends that I met in Sweden and all the colleagues in our unit. Special thanks go to Yezhe Lyu, Fangfei Sui, and Huijun Wang, for being with me during almost the whole Ph.D. journey.

China Scholarship Council is thanked for the financial support of my stay in Sweden. Olle Eriksson, Axel Hultgren and STT foundations are also acknowledged for funding the travels and studies.

Finally, I would like to express my great gratitude to my parents for their support, encouragement and understanding.

Ye Tian

Stockholm, May, 2018



# BIBLIOGRAPHY

- [1] J.K.L. Lai, C.H. Shek, K.H. Lo, *Stainless steels: An introduction and their recent developments*, Bentham Science Publishers, 2012.
- [2] K.H. Lo, C.H. Shek, J.K.L. Lai, *Recent developments in stainless steels*, *Mater. Sci. Eng. R Reports*. 65 (2009) 39–104.
- [3] Outokumpu, *Handbook of stainless steel*, 2013.
- [4] S. Lozano-Perez, *A guide on FIB preparation of samples containing stress corrosion crack tips for TEM and atom-probe analysis*, *Micron*. 39 (2008) 320–328.
- [5] C. Herrera, D. Ponge, D. Raabe, *Design of a novel Mn-based 1GPa duplex stainless TRIP steel with 60% ductility by a reduction of austenite stability*, *Acta Mater*. 59 (2011) 4653–4664.
- [6] F. Forouzan, A. Najafizadeh, A. Kermanpur, A. Hedayati, R. Surkialiabad, *Production of nano/submicron grained AISI 304L stainless steel through the martensite reversion process*, *Mater. Sci. Eng. A*. 527 (2010) 7334–7339.
- [7] Z. Li, K.G. Pradeep, Y. Deng, D. Raabe, C.C. Tasan, *Metastable high-entropy dual-phase alloys overcome the strength–ductility trade-off*, *Nature*. (2016) 4–11.
- [8] M.-M. Wang, C.C. Tasan, D. Ponge, A.-C. Dippel, D. Raabe, *Nanolaminate transformation-induced plasticity–twinning-induced plasticity steel with dynamic strain partitioning and enhanced damage resistance*, *Acta Mater*. 85 (2015) 216–228.
- [9] D. Raabe, D. Ponge, O. Dmitrieva, B. Sander, *Designing ultrahigh strength steels with good ductility by combining transformation induced plasticity and martensite aging*, *Adv. Eng. Mater*. 11 (2009) 547–555.
- [10] R. Blondé, E. Jimenez-Melero, L. Zhao, J.P. Wright, E. Brück, S. van der Zwaag, N.H. van Dijk, *High-energy X-ray diffraction study*

- on the temperature-dependent mechanical stability of retained austenite in low-alloyed TRIP steels, *Acta Mater.* 60 (2012) 565–577.
- [11] P. Hedström, T.S. Han, U. Lienert, J. Almer, M. Odén, Load partitioning between single bulk grains in a two-phase duplex stainless steel during tensile loading, *Acta Mater.* 58 (2010) 734–744.
- [12] B. Clausen, *Characterisation of polycrystal deformation*, Riso National Laboratory, Roskilde, Denmark, 1997.
- [13] E. Jimenez-Melero, N.H. van Dijk, L. Zhao, J. Sietsma, J.P. Wright, S. van der Zwaag, In situ synchrotron study on the interplay between martensite formation, texture evolution and load partitioning in low-alloyed TRIP steels, *Mater. Sci. Eng. A.* 528 (2011) 6407–6416.
- [14] O. Grässel, L. Krüger, G. Frommeyer, L.W. Meyer, High strength Fe-Mn-(Al, Si) TRIP/TWIP steels development - properties - application, *Int. J. Plast.* 16 (2000) 1391–1409.
- [15] E. Jimenez-Melero, N.H. van Dijk, L. Zhao, J. Sietsma, S.E. Offerman, J.P. Wright, S. van der Zwaag, Characterization of individual retained austenite grains and their stability in low-alloyed TRIP steels, *Acta Mater.* 55 (2007) 6713–6723.
- [16] K. Spencer, M. Véron, K. Yu-Zhang, J.D. Embury, The strain induced martensite transformation in austenitic stainless steels: Part 1 – Influence of temperature and strain history, *Mater. Sci. Technol.* 25 (2009) 7–17.
- [17] H.K.D.H. Bhadeshia, TRIP-Assisted Steels?, *ISIJ Int.* 42 (2002) 1059–1060.
- [18] G.W. Greenwood, R.H. Johnson, The deformation of metals under small stresses during phase transformations, *Proc. R. Soc. A Math. Phys. Eng. Sci.* 283 (1965) 403–422.
- [19] V.F. Zackay, E.R. Parker, D. Fahr, R. Busch, The enhancement of ductility in high-strength steels., *ASM Trans Quart.* 60 (1967) 252–259.
- [20] P.J. Jacques, J. Ladriere, F. Delannay, On the influence of

- interactions between phases on the mechanical stability of retained austenite in transformation-induced plasticity multiphase steels, *Metall. Mater. Trans. A Phys. Metall. Mater. Sci.* 32 (2001) 2759–2768.
- [21] E. Schmid, W. Boas, *Plasticity of crystals*, F. A. Hughes Co.Limited. (1950).
- [22] P. Hedström, U. Lienert, J. Almer, M. Odén, Elastic strain evolution and  $\epsilon$ -martensite formation in individual austenite grains during in situ loading of a metastable stainless steel, *Mater. Lett.* 62 (2008) 338–340.
- [23] Y. Tian, O.I. Gorbatov, A. Borgenstam, A. V. Ruban, P. Hedström, Deformation microstructure and deformation-induced martensite in austenitic Fe-Cr-Ni alloys depending on stacking fault energy, *Metall. Mater. Trans. A.* 48 (2017) 1–7.
- [24] S. Martin, S. Wolf, U. Martin, L. Krüger, D. Rafaja, Deformation mechanisms in austenitic TRIP/TWIP steel as a function of temperature, *Metall. Mater. Trans. A.* 47 (2014) 49–58.
- [25] F. Lecroisey, A. Pineau, Martensitic transformations induced by plastic deformation in the Fe-Ni-Cr-C system, *Metall. Trans.* 3 (1972) 391–400.
- [26] L. Remy, A. Pineau, Twinning and strain-induced f.c.c.  $\rightarrow$  h.c.p. transformation on the mechanical properties of CoNiCrMo alloys, *Mater. Sci. Eng.* 28 (1977) 99–107.
- [27] J. Talonen, H. Hänninen, Formation of shear bands and strain-induced martensite during plastic deformation of metastable austenitic stainless steels, *Acta Mater.* 55 (2007) 6108–6118.
- [28] N. Gey, B. Petit, M. Humbert, Electron backscattered diffraction study of  $\epsilon/\alpha'$  martensitic variants induced by plastic deformation in 304 stainless steel, *Metall. Mater. Trans. A.* 36 (2005) 3291–3299.
- [29] H.W. Zhang, Z.K. Hei, G. Liu, J. Lu, K. Lu, Formation of nanostructured surface layer on AISI 304 stainless steel by means of surface mechanical attrition treatment, *Acta Mater.* 51 (2003) 1871–1881.
- [30] N. Jia, R. Lin Peng, Y.D. Wang, S. Johansson, P.K. Liaw,

- Micromechanical behavior and texture evolution of duplex stainless steel studied by neutron diffraction and self-consistent modeling, *Acta Mater.* 56 (2008) 782–793.
- [31] B.L. Ennis, E. Jimenez-Melero, E.H. Atzema, M. Krugla, M.A. Azeem, D. Rowley, D. Daisenberger, D.N. Hanlon, P.D. Lee, Metastable austenite driven work-hardening behaviour in a TRIP-assisted dual phase steel, *Int. J. Plast.* 88 (2017) 126–139.
- [32] G. Bao, J.W. Hutchinson, R.M. McMeeking, The flow stress of dual-phase, non-hardening solids, *Mech. Mater.* 12 (1991) 85–94.
- [33] J. Talonen, Effect of strain-induced  $\alpha'$ -martensite transformation on mechanical properties of metastable austenitic stainless steels, Helsinki University of Technology, 2007.
- [34] S. Morito, H. Tanaka, R. Konishi, T. Furuhashi, T. Maki, The morphology and crystallography of lath martensite in Fe-C alloys, *Acta Mater.* 51 (2003) 1789–1799.
- [35] Y. Tian, U. Lienert, A. Borgenstam, T. Fischer, P. Hedström, Martensite formation during incremental cooling of Fe-Cr-Ni alloys: An in-situ bulk X-ray study of the grain-averaged and single-grain behavior, *Scr. Mater.* 136 (2017) 124–127.
- [36] Z. Nishiyama, *Martensitic transformation*, Elsevier, 2012.
- [37] M. Chen, S. Gao, D. Terada, A. Shibata, N. Tsuji, Characteristics of deformation induced martensite in SUS304 austenitic stainless steel deformed at RT and  $-60^{\circ}\text{C}$ , (2013) 563–569.
- [38] Y. Kim, T.-H. Ahn, D.-W. Suh, H.N. Han, Variant selection during mechanically induced martensitic transformation of metastable austenite by nanoindentation, *Scr. Mater.* 104 (2015) 13–16.
- [39] M. Humbert, B. Petit, B. Bolle, N. Gey, Analysis of the  $\gamma$ - $\epsilon$ - $\alpha'$  variant selection induced by 10% plastic deformation in 304 stainless steel at  $-60^{\circ}\text{C}$ , *Mater. Sci. Eng. A.* 454–455 (2007) 508–517.
- [40] Y. Higo, F. Lecroisey, T. Mori, Relation between applied stress and orientation relationship of  $\alpha'$  martensite in stainless steel single crystals, *Acta Metall.* 22 (1974) 313–323.
- [41] G. Olson, M. Cohen, A mechanism for the strain-induced nucleation

- of martensitic transformations, *J. Less Common Met.* 28 (1972) 107–118.
- [42] M. Kato, T. Mori, Orientation of martensite formed in Fe-23Ni-5Cr crystals under uniaxial stress along [001], *Acta Metall.* 25 (1977) 951–956.
- [43] W.-S. Lee, C.-F. Lin, The morphologies and characteristics of impact-induced martensite in 304L stainless steel, *Scr. Mater.* 43 (2000) 777–782.
- [44] K.P. Staudhammer, L.E. Murr, S.S. Hecker, Nucleation and evolution of strain-induced martensitic (b.c.c.) embryos and substructure in stainless steel: A transmission electron microscope study, *Acta Metall.* 31 (1983) 267–274.
- [45] D. Hull, D.J. Bacon, *Introduction to dislocations*, 5th ed., Elsevier, 2011.
- [46] J.R. Patel, M. Cohen, Criterion for the action of applied stress in the martensitic transformation, *Acta Metall.* 1 (1953) 531–538.
- [47] T. Suzuki, H. Kojima, K. Suzuki, T. Hashimoto, S. Koike, M. Ichihara, Plastic deformation and martensitic transformation in an iron-base alloy, *Scr. Metall.* 10 (1976) 353–358.
- [48] C.M. Wayman, H.K.D.H. Bhadeshia, *Phase transformations, nondiffusive*, Fourth Edi, 1996.
- [49] R.H. Richman, G.F. Bolling, Stress, deformation, and martensitic transformation, *Metall. Mater. Trans. B.* 2 (1971) 2451–2462.
- [50] G.B. Olson, M. Cohen, Kinetics of strain-induced martensitic nucleation, *Metall. Trans. A.* 6 (1975) 791–795.
- [51] L. Murr, K. Staudhammer, S. Hecker, Effects of strain state and strain rate on deformation-induced transformation in 304 stainless steel: Part II. Microstructural study, *Metall. Trans. A.* 13 (1982).
- [52] A. Sato, M. Kato, Y. Sunaga, T. Miyazaki, T. Mori, Stress induced martensitic transformation in Fe-Ni-C alloy single crystals, *Acta Metall.* 28 (1979) 367–376.
- [53] N. Nakada, H. Ito, Y. Matsuoka, T. Tsuchiyama, S. Takaki, Deformation-induced martensitic transformation behavior in cold-

- rolled and cold-drawn type 316 stainless steels, *Acta Mater.* 58 (2010) 895–903.
- [54] L. Remy, Temperature variation of the intrinsic stacking fault energy of a high manganese austenitic steel, *Acta Metall.* 25 (1977) 173–179.
- [55] R.E. Schramm, R.P. Reed, Stacking fault energies of seven commercial austenitic stainless steels, *Metall. Trans. A.* 6 (1975) 1345–1351.
- [56] Y. Tian, A. Borgenstam, P. Hedström, A microstructural investigation of athermal and deformation-induced martensite in Fe-Cr-Ni alloys, *Mater. Today Proc.* 2 (2015) 687–690.
- [57] G.B. Olson, M. Cohen, A general mechanism of martensitic nucleation: Part I. General concepts and the FCC → HCP transformation, *Metall. Trans. A.* 7 (1976) 1897–1904.
- [58] J. Andersson, T. Helander, L. Höglund, Thermo-Calc & DICTRA, computational tools for materials science, *Calphad.* 26 (2002) 273–312.
- [59] T.S. Byun, E.H. Lee, J.D. Hunn, Plastic deformation in 316LN stainless steel – characterization of deformation microstructures, *J. Nucl. Mater.* 321 (2003) 29–39.
- [60] S. Curtze, V.T. Kuokkala, Dependence of tensile deformation behavior of TWIP steels on stacking fault energy, temperature and strain rate, *Acta Mater.* 58 (2010) 5129–5141.
- [61] K. Nohara, Y. Ono, N. Ohashi, Composition and grain size dependencies of strain-induced martensitic transformation in metastable austenitic stainless steels, *J. Iron Steel Inst. Japan.* 63 (1977) 772–782.
- [62] Y. Matsuoka, T. Iwasaki, N. Nakada, T. Tsuchiyama, S. Takaki, Effect of grain size on thermal and mechanical stability of austenite in metastable austenitic stainless steel, *ISIJ Int.* 53 (2013) 1224–1230.
- [63] P.A. Shade, B. Blank, J.C. Schuren, T.J. Turner, P. Kenesei, K. Goetze, R.M. Suter, J. V. Bernier, S.F. Li, J. Lind, U. Lienert, J. Almer, A rotational and axial motion system load frame insert for

- in situ high energy x-ray studies, *Rev. Sci. Instrum.* 86 (2015).
- [64] A.C. Narváez, I.G.C. Weppelman, R.J. Moerland, N. Liv, A.C. Zonneville, P. Kruit, J.P. Hoogenboom, Cathodoluminescence microscopy of nanostructures on glass substrates, *Opt. Express.* 21 (2013) 29968.
- [65] P. Goodhew, J. Humphreys, R. Beanland, *Electron microscopy and analysis*, Third Ed., CRC Press, London, 2001.
- [66] R. Borrajo-Pelaez, P. Hedström, Recent developments of crystallographic analysis methods in the scanning electron microscope for applications in metallurgy, *Crit. Rev. Solid State Mater. Sci.* (2017) 1–20.
- [67] S. Zaefferer, N.-N. Elhami, Theory and application of electron channelling contrast imaging under controlled diffraction conditions, *Acta Mater.* 75 (2014) 20–50.
- [68] D. Dingley, Progressive steps in the development of electron backscatter diffraction and orientation imaging microscopy, *J. Microsc.* 213 (2004) 214–224.
- [69] R.P. Babu, S. Irukuvarghula, A. Harte, M. Preuss, Nature of gallium focused ion beam induced phase transformation in 316L austenitic stainless steel, *Acta Mater.* 120 (2016) 391–402.
- [70] <https://www.mpie.de/3077954/EBSD>, (n.d.).
- [71] <http://mtex-toolbox.github.io/>, (n.d.).
- [72] G. Nolze, R. Hielscher, Orientations - Perfectly colored, *J. Appl. Crystallogr.* 49 (2016) 1786–1802.
- [73] H.C. Pollock, The discovery of synchrotron radiation, *Am J. Phys.* 51 (1983) 278.
- [74] <http://www.esrf.eu/about/synchrotron-science/history-synchrotron>, (n.d.).
- [75] D.H. Bilderback, P. Elleaume, E. Weckert, Review of third and next generation synchrotron light sources, *J. Phys. B At. Mol. Opt. Phys.* 38 (2005).
- [76] <http://www.esrf.eu/about/ask-an-expert/questions-answers>, (n.d.).

- [77] N. Jia, Z.H. Cong, X. Sun, S. Cheng, Z.H. Nie, Y. Ren, P.K. Liaw, Y.D. Wang, An in situ high-energy X-ray diffraction study of micromechanical behavior of multiple phases in advanced high-strength steels, *Acta Mater.* 57 (2009) 3965–3977.
- [78] N. Li, Y.D. Wang, W.J. Liu, Z.N. An, J.P. Liu, R. Su, J. Li, P.K. Liaw, In situ X-ray microdiffraction study of deformation-induced phase transformation in 304 austenitic stainless steel, *Acta Mater.* 64 (2014) 12–23.
- [79] O. Muránsky, P. Šittner, J. Zrník, E.C. Oliver, In situ neutron diffraction investigation of the collaborative deformation–transformation mechanism in TRIP-assisted steels at room and elevated temperatures, *Acta Mater.* 56 (2008) 3367–3379.
- [80] E. Cakmak, H. Choo, K. An, Y. Ren, A synchrotron X-ray diffraction study on the phase transformation kinetics and texture evolution of a TRIP steel subjected to torsional loading, *Acta Mater.* 60 (2012) 6703–6713.
- [81] R. Blondé, E. Jimenez-Melero, L. Zhao, N. Schell, E. Brück, S. van der Zwaag, N.H. van Dijk, The mechanical stability of retained austenite in low-alloyed TRIP steel under shear loading, *Mater. Sci. Eng. A.* 594 (2014) 125–134.
- [82] N. Van Dijk, A. Butt, L. Zhao, J. Sietsma, S. Offerman, J. Wright, S. Vanderzwaag, Thermal stability of retained austenite in TRIP steels studied by synchrotron X-ray diffraction during cooling, *Acta Mater.* 53 (2005) 5439–5447.
- [83] E. Jimenez-Melero, N.H. van Dijk, L. Zhao, J. Sietsma, S.E. Offerman, J.P. Wright, S. van der Zwaag, The effect of aluminium and phosphorus on the stability of individual austenite grains in TRIP steels, *Acta Mater.* 57 (2009) 533–543.
- [84] B.H. Toby, R.B. Von Dreele, GSAS-II: The genesis of a modern open-source all purpose crystallography software package, *J. Appl. Crystallogr.* 46 (2013) 544–549.
- [85] A.K. De, D.C. Murdock, M.C. Mataya, J.G. Speer, D.K. Matlock, Quantitative measurement of deformation-induced martensite in 304 stainless steel by X-ray diffraction, *Scr. Mater.* 50 (2004) 1445–1449.

- [86] M.J. Dickson, The Significance of Texture Parameters in Phase Analysis By X-Ray Diffraction, *J. Appl. Crystallogr.* 2 (1969) 176–180.
- [87] I.C. Noyan, J.B. Cohen, Residual stress: measurement by diffraction and interpretation, Springer, 2013.
- [88] S. Matthies, H.G. Priesmeyer, M.R. Daymond, On the diffractive determination of single-crystal elastic constants using polycrystalline samples, *J. Appl. Crystallogr.* 34 (2001) 585–601.
- [89] B.E. Warren, X-ray diffraction, Dover Publications Inc., New York, 1990.
- [90] S. Martin, C. Ullrich, D. Imek, U. Martin, D. Rafaja, Stacking fault model of-martensite and its DIFFaX implementation, *J. Appl. Crystallogr.* 44 (2011) 779–787.
- [91] L. Lutterotti, R. Vasin, H.-R. Wenk, Rietveld texture analysis from synchrotron diffraction images. I. Calibration and basic analysis, *Powder Diffr.* 29 (2014) 76–84.
- [92] H.-R. Wenk, L. Lutterotti, P. Kaercher, W. Kaniitpanyacharoen, L. Miyagi, R. Vasin, Rietveld texture analysis from synchrotron diffraction images. II. Complex multiphase materials and diamond anvil cell experiments, *Powder Diffr.* 29 (2014) 220–232.
- [93] N.C. Popa, The (hkl) dependence of diffraction-line broadening caused by strain and size for all Laue groups in rietveld refinement, *J. Appl. Crystallogr.* 31 (1998) 176–180.
- [94] H.F. Poulsen, 3DXRD – a new probe for materials science, Roskilde: Risø National Laboratory, 2004.
- [95] H.F. Poulsen, An introduction to three-dimensional X-ray diffraction microscopy, *J. Appl. Crystallogr.* 45 (2012) 1084–1097.
- [96] S. Schmidt, GrainSpotter: A fast and robust polycrystalline indexing algorithm, *J. Appl. Crystallogr.* 47 (2014) 276–284.
- [97] <http://docplayer.net/58812907-Near-field-mapping-with-box-beam-using-fable-and-grainsweeper-3d.html>, (n.d.).
- [98] P.W. Trimby, Y. Cao, Z. Chen, S. Han, K.J. Hemker, J. Lian, X. Liao, P. Rottmann, S. Samudrala, J. Sun, J.T. Wang, J. Wheeler,

- J.M. Cairney, Characterizing deformed ultrafine-grained and nanocrystalline materials using transmission Kikuchi diffraction in a scanning electron microscope, *Acta Mater.* 62 (2014) 69–80.
- [99] T.B. Britton, A.J. Wilkinson, High resolution electron backscatter diffraction measurements of elastic strain variations in the presence of larger lattice rotations, *Ultramicroscopy.* 114 (2012) 82–95.